Nanoscale

ROYAL SOCIETY OF CHEMISTRY

PAPER

View Article Online
View Journal | View Issue

Check for updates

Cite this: *Nanoscale*, 2024, **16**, 8390

Scalable solid-state synthesis of 2D transition metal oxide/graphene hybrid materials and their utilization for microsupercapacitors†

Muxuan Yang, Pratik Kasbe, Jinyu Bu and Weinan Xu *

School of Polymer Science and Polymer Engineering, The University of Akron, Akron, OH 44325, USA. E-mail: weinanxu@uarkon.edu

Two-dimensional metal oxide (MO) nanostructures have unique properties compared with their bulk or 0D and 1D (nanoparticle and nanowire) counterparts. Their abundant surface area and atomically thin 2D structure are advantageous for their applications in catalysis and energy, as well as integration with 2D layered materials such as graphene and reduced graphene oxide (rGO). However, fast and scalable synthesis of 2D MOs and their nanocomposites remains challenging. Here, we developed a microwave-assisted solid-state synthesis method for the scalable generation of 2D MOs and 2D MO/rGO nanocomposites with tunable structure and composition. The structures and properties of 2D Fe_2O_3 and 2D ZnO as well as their nanocomposites with rGO were systematically investigated. The excellent electrochemical properties of such 2D MO/rGO nanocomposites also enable us to use them as electrode materials to fabricate microsupercapacitors. This work provides new insights into the scalable and solid-state synthesis of 2D nanocomposites and their potential applications in catalysis, energy conversion and storage.

Received 8th February 2024,
Accepted 27th March 2024

DOI: 10.1039/d4nr00587b

rsc.li/nanoscale

1. Introduction

With the ever-increasing demand for energy and the pressing need for sustainable energy sources, the development of high-performance energy storage devices has become of great importance.[1–3] These devices, including batteries and supercapacitors, are not only essential for storing energy from renewable sources like solar and wind, but also critical for powering up electric vehicles and consumer electronics.[4–6] Supercapacitor is a type of electrochemical energy storage device that has attracted significant attention in industry and academia. They are capable of delivering high power density, fast charge/discharge, and long cycling stability.[7] However, their major limitation is their relatively low energy density when compared to rechargeable batteries. The development of new electrode materials with enhanced performance is of critical importance to overcome such limitations.[8]

Based on the energy storage mechanisms of supercapacitors, they can be classified into two types: electrochemical double-layer capacitors (EDLCs) and pseudocapacitive capacitors. The difference mainly comes from their behavior at the electrode/electrolyte interface. EDLCs are mainly based on carbonaceous electrode materials, and they achieve separation of charges in a Helmholtz double layer at the electrode/electrolyte interface. Pseudocapacitance is achieved by faradaic electron charge transfer with redox reactions, intercalation or electrosorption. The corresponding electrode materials (metal oxides/hydroxides or

Weinan Xu

Dr. Weinan Xu joined the School of Polymer Science and Polymer Engineering at the University of Akron as an assistant professor in 2019. He received his Ph.D. degree in Materials Science and Engineering from Georgia Institute of Technology and did postdoctoral research at Johns Hopkins University. His current research focuses on the development of functional polymer nanocomposites and their advanced manufacturing, with applications in biomedicine, electronics, and energy storage. He has been recognized with several awards, including the Polymer Processing Society Early Career Award, DARPA Young Faculty Award, and Best Ph.D. Thesis Award from Sigma Xi and Georgia Tech.

---

† Electronic supplementary information (ESI) available. See DOI: **https://doi.org/10.1039/d4nr00587b**

conductive polymers) usually have the ability to provide higher specific capacitance.[9,10]

Transition metal oxides (MO) have emerged as important electrode materials for supercapacitors due to their tunable valency, high theoretical capacitance, abundance in nature, resistance to corrosion and good thermal stability.[11,12] The combination of transition metal oxides with carbon nanomaterials (especially graphene and reduced graphene oxide (rGO)) to form hybrids or nanocomposites is a promising strategy to further enhance their energy storage performance due to the synergy between EDLCs and pseudocapacitance mechanisms.[13–17] Most of the previous reports involve physical mixing or blending of MO nanostructures with graphene. The MO nanostructures are usually in the form of 0D nanoparticles or 1D nanorods and nanowires. Their synthesis is also primarily based on sol–gel, hydrothermal/solvothermal, and vapor phase deposition,[18–21] which are time-consuming, expensive, and not scalable.[22–25]

Because of the 2D atomically thin nature of graphene, it is expected to have stronger and more intimate interactions with MOs if the MOs also have 2D atomically thin structures. The abundant contact area and strong van der Waals interaction between graphene and 2D MOs will lead to synergistic property enhancement.[26–29] There are several pioneering works on the synthesis and characterization of 2D MOs. For instance, 2D iron oxide (Fe_2O_3) was synthesized by liquid exfoliation in dimethylformamide from natural ore hematite (α-Fe_2O_3) and named hematene.[30] Exfoliation of 2D Fe_2O_3 in melamine aqueous solution under mild sonication was also reported.[31] Chahal *et al.* developed a microwave-assisted synthesis of 2D MOs in dimethylformamide or isopropanol solvent using metal chlorides as precursors.[32] These 2D MOs have already been investigated for applications including catalysis,[30–33] optics,[34,35] electronics,[36,37] and sensing.[38,39] However, scalable and solid-state synthesis of 2D MO/rGO nanocomposites and their utilization in energy storage have not been demonstrated before.

To fill this knowledge gap, in this work, we developed a microwave-assisted solid-state synthesis approach for 2D MOs and 2D MO/rGO nanocomposites. Our approach is simple, fast, and scalable. Two different 2D MOs (Fe_2O_3 and ZnO) and their rGO nanocomposites were prepared and systematically investigated. The electrochemical properties of 2D MO/rGO nanocomposites were studied and they showed excellent performance. We also used the 2D Fe_2O_3/rGO nanocomposites as the main electrode materials to fabricate symmetric and asymmetric microsupercapacitors (MSCs). Our research provides a versatile and important platform for the scalable synthesis of 2D MO/rGO nanocomposites and their use in energy storage.

2. Experimental

2.1 Materials

Graphite flakes, polyvinyl alcohol (PVA), zinc chloride ($ZnCl_2$), potassium hydroxide (KOH) and potassium permanganate ($KMnO_4$) were purchased from Sigma Aldrich. Anhydrous iron chloride ($FeCl_3$) was purchased from Thermo Scientific. Ethanol, and sulfuric acid (H_2SO_4) were purchased from Fisher. Hydrogen peroxide (H_2O_2) was purchased from VWR Chemicals. GO was synthesized using a modified Hummers' method.[40] The obtained GO suspension was directly freeze-dried for future use. Electrochemically exfoliated graphene (EG) was prepared by using expanded graphite as the working electrode and a platinum wire as the counter electrode in 0.1 M H_2SO_4 electrolyte under a 10 V bias. The exfoliated material was collected and washed with deionized (DI) water by vacuum filtration, and then sonicated to further separate the graphene flakes.

2.2 Solid-state synthesis of 2D MOs and 2D MO/rGO nanocomposites

The 2D Fe_2O_3 was synthesized using a microwave-assisted method in solid state. Specifically, $FeCl_3$ powder was placed in a glass Petri dish and placed inside a microwave furnace at 1000 W power for 20 s, and then cooled down for 1 minute to prevent overheating. Such a process was repeated 10 times (total microwave time: 200 s). Then the obtained red-brownish product was collected and washed with water to remove the excess metal precursors. Subsequently, the product was dispersed in ethanol and subjected to sonication (10 minutes probe sonication followed by 1 hour bath sonication) to obtain the final 2D Fe_2O_3.

For the synthesis of 2D Fe_2O_3/rGO nanocomposites, $FeCl_3$ powder was first mixed with graphene oxide in a calculated mass ratio, and then the mixture was used for the same microwave-assisted synthesis and washing processes as described above. The synthesis of 2D ZnO/rGO nanocomposites follows a similar procedure by using $ZnCl_2$ as the metal precursor. The weight ratio of metal chloride and GO in the mixture can be tuned to control the final composition of the 2D nanocomposites.

2.3 Fabrication of microsupercapacitors

Two approaches were used for the fabrication of MSCs based on the 2D Fe_2O_3/rGO nanocomposites as electrode materials. The first approach is based on photolithography and vacuum filtration, which produces arrays of symmetric MSCs. Specifically, a nylon filter membrane was used as the substrate. A photolithography pattern with the opposite geometry of the interdigitated electrodes was generated on a nylon filter membrane with an SU-8 photoresist. Such a patterned filter membrane was then used for vacuum filtration so that the electrode materials would be deposited only within the pattern. EG was deposited as the first layer (0.001 mg mm^{-2}) and acted as a metal-free current collector. Then the 2D Fe_2O_3/rGO nanocomposites (0.004 mg mm^{-2}) were deposited on top of the EG layer. Lastly, a conductive silver paste layer (0.002 mg mm^{-2}) was deposited on top to generate good electrical contact with copper wires. After the fabrication process, the SU-8 pattern was removed and the MSC was completely dried in a vacuum oven. The gel electrolyte used was KOH/PVA, which was prepared by dissolving 1 g of KOH in 5 ml of DI water and 1 g of PVA in 10 ml of DI water and mixed them together. The KOH/PVA was used a gel electrolyte for the solid-state MSCs.

The second approach for MSC fabrication is based on laser cutting and spray coating, which allows the fabrication of asymmetric MSCs. Laser cutting was used to create a polyester shadow mask for spray coating of the electrode materials with a commercial handheld airbrush. A controlled amount of the ethanol suspension of 2D Fe_2O_3/rGO nanocomposites was spray-coated through the shadow mask on a preheated (130 °C) polyimide substrate and a calculated amount of EG was added to the ink as a conductive additive. Then another shadow mask was used for the spray-coating of EG on the polyimide substrate as the second electrode. The ink for the positive electrode contains 13.5 mg of 2D Fe_2O_3/rGO nanocomposites and 3.5 mg of EG. The ink for the negative electrode contains 17.5 mg of EG. Subsequently, the KOH/PVA gel electrolyte was applied to the electrodes to complete the device fabrication.

2.6 Characterization

SEM was conducted with a JEOL-7401 FE-SEM. TEM (FEI Tecnai F20 S) was used to obtain high-resolution images. X-ray diffraction (XRD) was conducted with an Ultima IV X-ray diffractometer (Rigaku, Tokyo, Japan) operated at 40 kV and 35 mA with a Cu Kα energy frequency (wavelength of 1.54 Å). X-ray photoelectron spectroscopy (XPS) was performed using a PHI 5000 Versaprobe II system. Raman Spectroscopy was carried out using a Renishaw inVia confocal Raman. UV-Vis spectroscopy was performed using a HP 8453 UV-Vis absorption spectrometer.

Electrochemical measurements were performed in both 3-electrode and 2-electrode systems. For the 3-electrode test, the working electrode was prepared by mixing the active material, carbon black and polyvinylidene fluoride (PVDF) in a mass ratio of 90 : 5 : 5 to make a slurry, then it was coated onto Ni foam, followed by drying in a vacuum oven. KOH solution (1M) was used as the electrolyte, Ag/AgCl was used as the reference electrode, and a platinum wire was used as the counter electrode.

All the measurements were carried out using a CHI 660D electrochemical workstation. Cyclic voltammetry (CV) was performed at different scan rates ranging from 1 mV s^{-1} to 100 mV s^{-1}. Galvanostatic charge and discharge (GCD) curves were recorded at different current densities from 1 mA cm^{-2} to 10 mA cm^{-2}. Electrochemical impedance spectroscopy (EIS) was performed between a frequency range of 0.1 Hz and 1 MHz. The capacitance calculation equation used can be seen in the ESI.†

3. Results and discussion

3.1 Solid-state synthesis of 2D MOs and their nanocomposites

The schematic representation of our solid-state synthesis of 2D MO/rGO nanocomposites and their application as electrode materials for energy storage devices is shown in Fig. 1. The solid-state synthesis approach uses metal chlorides as metal precursors and GO as the microwave absorber and conductive component after its reduction. The high energy generated by microwaves induces the chemical conversion of metal chlorides to metal oxides, and at the same time, reduces GO into rGO. After the microwave-assisted synthesis, the products were further purified by washing and exfoliated by sonication in ethanol. We used this approach to synthesize two types of 2D MOs (2D Fe_2O_3 and ZnO) and their nanocomposites with rGO.

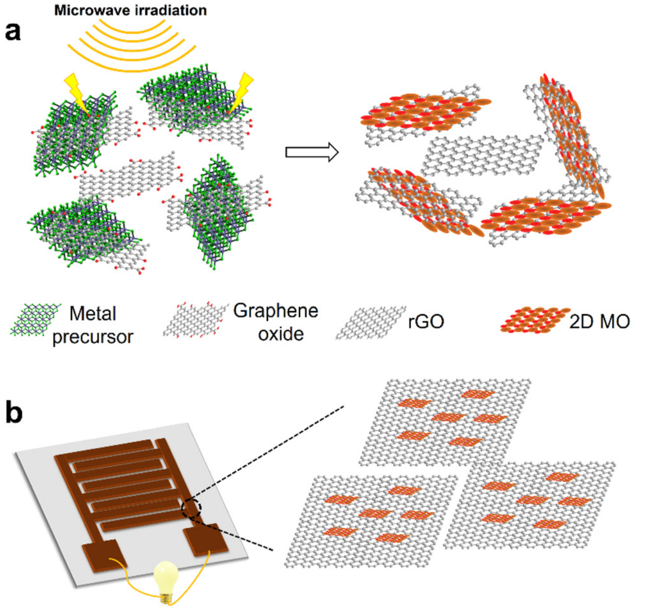

Fig. 1 (a) Schematic of the microwave-assisted solid-state synthesis of 2D MO/rGO nanocomposites. (b) Utilization of 2D MO/rGO nanocomposites as electrodes for the fabrication of energy storage devices such as microsupercapacitors.

Microwave irradiation contains both the electric field and magnetic field that act normal to each other. The metal chloride precursors absorb electromagnetic energy and convert it into thermal energy, which can be further enhanced with the incorporation of GO. Such a local high thermal energy can rapidly break the metal chloride bonds when the thermal energy exceeds the bond dissociation energy.[32] The oxygen molecules from air are also excited by microwave irradiation and generate radicals, which react with activated metal atoms to form metal oxides.[32,41] The small amount of moisture in air can also participate in the reaction.[42] The probable reaction equations are: $4FeCl_3 + 3O_2 \rightarrow 2Fe_2O_3 + 6Cl_2$; $FeCl_3 + H_2O \rightarrow FeOCl + 2HCl$; and $2FeOCl + H_2O \rightarrow Fe_2O_3 + 2HCl$ (for 2D Fe_2O_3). And $2ZnCl_2 + O_2 \rightarrow 2ZnO + 2Cl_2$; $ZnCl_2 + H_2O \rightarrow Zn(OH)Cl + HCl$; and $Zn(OH)Cl \rightarrow ZnO + HCl$ (for 2D ZnO).

The exact mechanism for the formation of 2D metal oxides under such a condition requires further investigation. Our hypothesis is that the electric field from microwave irradiation acts in a static plane (with sinusoidal magnitude over time) facilitates the atom rearrangement in a 2D plane. In addition, the incorporation of 2D GO nanosheets can act as an atomically thin 2D template to further promote 2D MO formation.

We estimated the yield of such a solid-state synthesis of 2D Fe_2O_3 and ZnO by measuring the ratio of the actual product weight and the theoretical amount. Without the incorporation of GO, the yield for 2D Fe_2O_3 is about 10.2%, and the yield increases to 36.0% when 10 wt% of GO is incorporated into the precursors (GO has a 7 wt% weight loss during this reduction process, which was taken into consideration during the yield calculation). The yield for 2D ZnO under the same reaction conditions is lower (7.9%) due to the lower microwave absorption capability. Therefore, in the following discussion, we will focus on the 2D Fe_2O_3 and 2D Fe_2O_3 nanocomposites. We also varied the weight fraction of GO in the metal chloride precursors for the solid-state synthesis, for instance, the 2D Fe_2O_3/rGO (10/1) sample has the amount of GO equals to 10 wt% of iron chloride in the precursor and the 2D Fe_2O_3/rGO (20/1) sample has the amount of GO equals to 5 wt% of iron chloride in the precursor.

3.2 Characterization of 2D MOs and their nanocomposites

The morphologies of 2D Fe_2O_3 and the 2D Fe_2O_3/rGO (10/1) nanocomposite were studied by high-resolution electron microscopy. The SEM image of 2D Fe_2O_3 (Fig. 2a) shows a high density of nanoflakes, and some of them have a relatively large aspect ratio. AFM characterization (Fig. 2b and c) of a more diluted sample shows that 2D Fe_2O_3 has the lateral size generally below 500 nm and an average thickness of 10.0 nm from the cross-section analysis. Such a thickness indicates that most of the 2D Fe_2O_3 nanosheets have a few-layer (<10) structure. TEM image (Fig. 2d) of 2D Fe_2O_3 shows their lateral size in the range of 100–500 nm. From high-resolution TEM (Fig. 2e and f), well-defined lattice fringes can be observed with a lattice spacing of 0.35 nm.

The SEM image (Fig. 2g) of the 2D Fe_2O_3/rGO (10/1) nanocomposite shows that it has a nanosheet morphology with lateral sizes in the range of 100–800 nm. The TEM image (Fig. 2h) shows that domains of higher contrast which correspond to 2D Fe_2O_3 are on the surface of rGO nanosheets. The high-resolution TEM images (Fig. 2i–k) further show that these two domains have different crystalline structures: the one (Fig. 2k) with well-defined lattice fringes and a d spacing of 0.35 nm corresponds to 2D Fe_2O_3 and the other one with lower contrast and large spacing (0.44 nm) corresponds to the few-layer graphene domain. The SEM image of the 2D ZnO/rGO

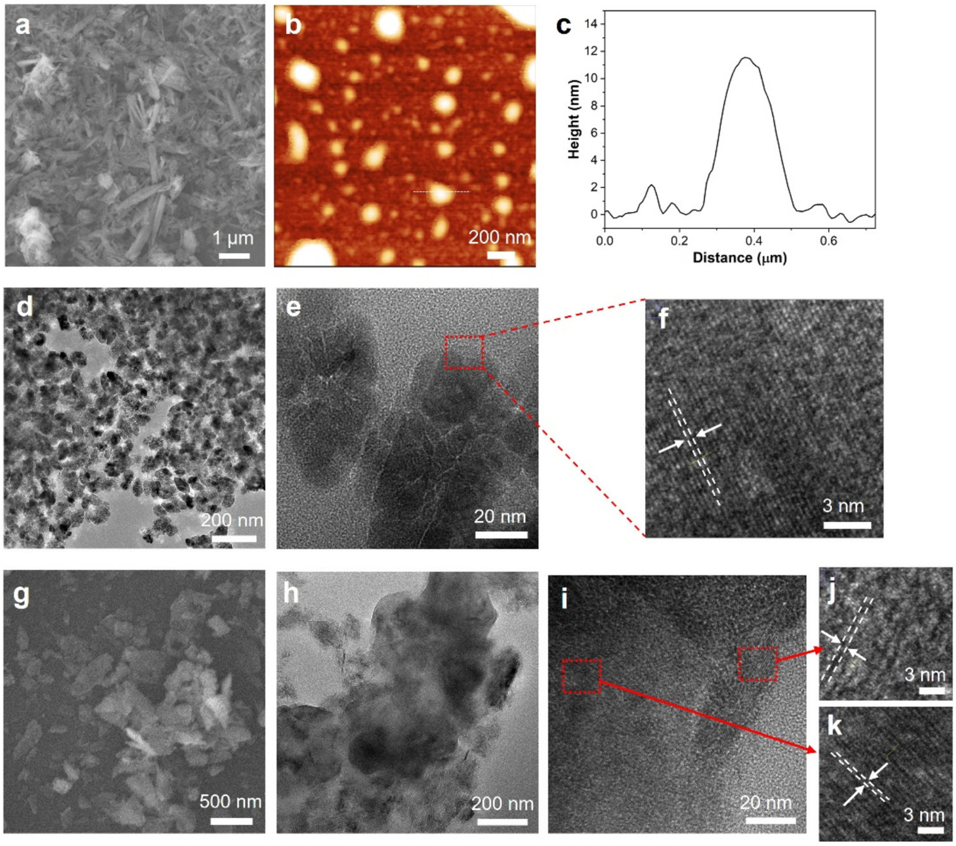

Fig. 2 Morphology and structural characterization of 2D Fe_2O_3 and the 2D Fe_2O_3/rGO (10/1) nanocomposite. (a) SEM image of 2D Fe_2O_3. (b and c) AFM image of 2D Fe_2O_3 and the representative thickness profile from cross-section measurement. (d and e) TEM images of 2D Fe_2O_3 at two different magnifications. (f) High-resolution TEM image of 2D Fe_2O_3 showing the lattice structure. (g) SEM image of the 2D Fe_2O_3/rGO nanocomposites. (h and i) TEM image of 2D Fe_2O_3/rGO at two different magnifications. (j and k) High-resolution TEM images of two different locations on 2D Fe_2O_3/rGO marked by red boxes in panel i.

nanocomposites shows a similar morphology (Fig. S1†) with 2D ZnO nanosheets dispersed on the surface of rGO flakes. The EDX spectrum (Fig. S1†) further confirms the existence of 2D ZnO nanosheets in the nanocomposites.

To further investigate the structure and properties of the 2D MOs and their nanocomposites, several types of spectroscopy and scattering were conducted. Raman spectroscopy was used to characterize the structures of 2D Fe_2O_3 and the 2D Fe_2O_3/rGO nanocomposites (Fig. 3a). Characteristic peaks of the α-phase of Fe_2O_3 can be clearly observed, including the peak at 224 cm^{-1} which corresponds to the A_{1g} mode and the peaks at 296, 410, and 613 cm^{-1} which correspond to the E_g mode, and the peak at 1315 cm^{-1} is attributed to two-magnon scattering.[43,44] Moreover, a forbidden disorder-originated vibrational peak at 650 cm^{-1} confirms the formation of 2D crystals since there is no such disorder in conventional 3D crystals.[45] In addition, the intensity ratio of A_{1g} and E_g peaks at 224 and 296 cm^{-1} was calculated to be 0.77, which further confirms the 2D nature of the synthesized Fe_2O_3 nanosheets, because a such ratio is larger than 1.0 for bulk crystals.[30] For the 2D Fe_2O_3/rGO nanocomposites, the major peaks for 2D Fe_2O_3 remain and the peaks corresponding to the G band and D band of rGO at 1570 and 1360 cm^{-1} can also be observed. It is noted that the peak at 1315 cm^{-1} has a substantially reduced intensity for the 2D Fe_2O_3/rGO nanocomposites, the probable reasons include the intimate contact between rGO and Fe_2O_3 leads to changes in the two-magnon interaction or the reduced FeOOH side product in the nanocomposites.[43]

We also characterized the 2D ZnO/rGO nanocomposites by Raman spectroscopy (Fig. S2†). The three characteristic graphene peaks, the D band (1360 cm^{-1}), G band (1570 cm^{-1}), and 2D band (2700 cm^{-1}), are present in the Raman spectrum. In addition, two peaks at 94 cm^{-1} and ~430 cm^{-1} are observed, which correspond to the E_2 vibration mode of ZnO.[46–48] The peaks from ZnO have relatively small intensity, which is due to the lower yield during the solid-state synthesis.

The crystalline structure was further investigated by XRD (Fig. 3b). 2D Fe_2O_3 shows all the characteristic peaks of α-Fe_2O_3 with a well-defined shape. For the 2D Fe_2O_3/rGO nanocomposite, besides all the peaks from α-Fe_2O_3, there is also an additional peak with a 2θ value of 26°, which corresponds to the (002) crystal plane of multilayered rGO.[49,50] This peak intensity is relatively low because rGO is the minor component in the 2D Fe_2O_3/rGO (10/1) nanocomposite.

The UV-vis spectrum of 2D Fe_2O_3 shows absorption peaks at 246, 365, and 551 nm (Fig. 3c). The optical adsorption spectrum can be used to estimate the band gap energy of 2D Fe_2O_3 by using the Tauc plot (Fig. 3c inset). The calculated band gap for our 2D Fe_2O_3 is 2.86 eV, which is consistent with literature reports. Such a band gap is larger than that of bulk Fe_2O_3 crystals due to the quantum effect when the size reduces to the nanoscale.[30,32,51] For the 2D Fe_2O_3/rGO nanocomposites (Fig. 3d), the peaks for 2D Fe_2O_3 at 246 and 365 nm can clearly be observed. There is also a strong peak at 221 nm, which corresponds to the absorption peak of rGO in the nanocomposites. The band gap calculation from the Tauc plot shows almost the same value (2.85 eV) as that of 2D Fe_2O_3.

XPS was conducted to confirm the structures and compositions of 2D Fe_2O_3 and the 2D Fe_2O_3/rGO nanocomposites. The survey scan (Fig. S3†) of the 2D nanocomposites shows

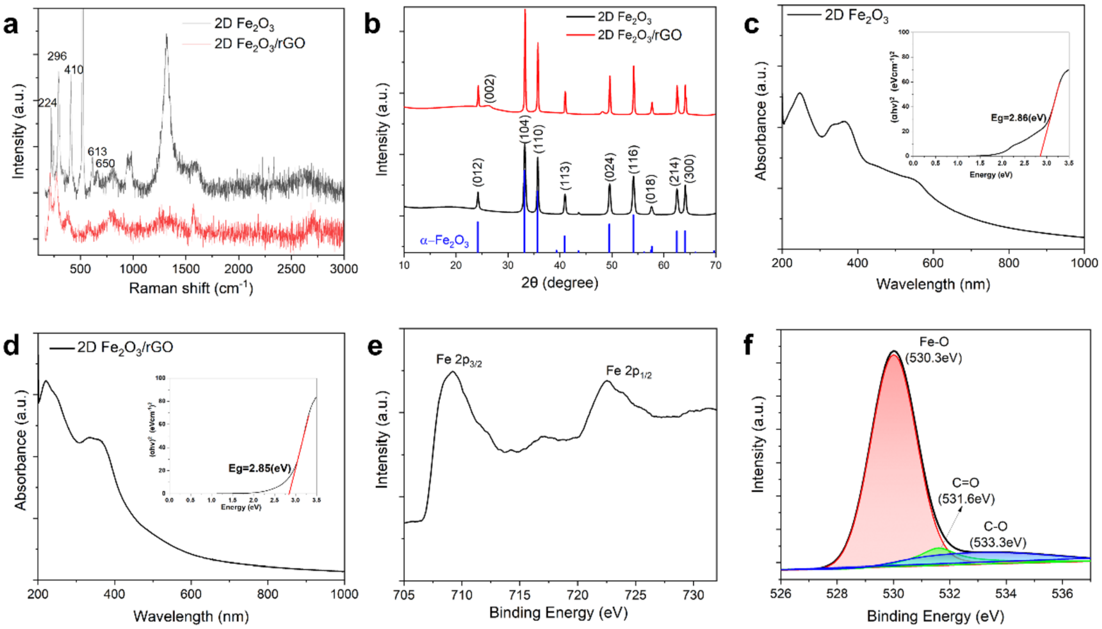

Fig. 3 Characterization of 2D Fe_2O_3 and the 2D Fe_2O_3/rGO (10/1) nanocomposite. (a) Raman spectra of 2D Fe_2O_3 and the 2D Fe_2O_3/rGO nanocomposites. (b) XRD spectra of 2D Fe_2O_3 and the 2D Fe_2O_3/rGO nanocomposites. (c and d) UV-vis spectra of 2D Fe_2O_3 and the 2D Fe_2O_3/rGO nanocomposites. The inset in each panel corresponds to the Tauc plot derived from the absorption data. (e) XPS spectrum of the Fe 2p peak for 2D Fe_2O_3. (f) XPS spectrum of the O 1s peak and its deconvolution for the 2D Fe_2O_3/rGO nanocomposites.

characteristic peaks of oxygen, iron, and carbon. The high-resolution scan of the Fe 2p peak (Fig. 3e) shows two distinct peaks located at 709.3 eV and 722.6 eV, corresponding to the two spin states of iron: Fe $2p_{3/2}$ and Fe $2p_{1/2}$, respectively.[32,52,53] The energy separation between the two peaks is 13.3 eV, which is consistent with previous reports on Fe_2O_3.[54] In addition, a satellite peak at 717.1 eV appears, which is characteristic of Fe^{3+} ions in Fe_2O_3,[55] this further confirms that the 2D iron oxide is primarily Fe_2O_3 rather than other forms such as Fe_3O_4.[56] The high-resolution scan of the O 1s peak and its deconvolution (Fig. 3f) shows three sub-peaks, the major one at 530.3 eV is attributed to the lattice oxygen involved in the binding of α-Fe_2O_3 and two minor peaks at 531.6 eV and 533.3 eV primarily correspond to the residue surface oxygen groups including C═O and C–O from rGO.[57,58]

3.3 Electrochemical properties of 2D MOs and their nanocomposites

Our nanocomposites composed of *in situ* synthesized 2D metal oxides integrated with graphene have the potential to be high-performance materials for energy storage applications due to their combination of electrochemical activity and conductivity. We first investigated the electrochemical performance of the 2D MO/rGO nanocomposites in a three-electrode setup. The 2D MO/rGO nanocomposites were mixed with PVDF as a binder and carbon black as a conductive filler (with a mass ratio of 90 : 5 : 5) to form a slurry, which was then coated on nickel foam as the working electrode. The reference electrode was Ag/AgCl and the counter electrode was a platinum wire, and 1 M KOH was used as the liquid electrolyte.

CV scans of the 2D Fe_2O_3/rGO (10/1) nanocomposite at scan rates from 5 mV s^{-1} to 50 mV s^{-1} are shown in Fig. 4a. The curves display a pair of typical redox peaks corresponding to the valence state change of iron between Fe^{3+} and Fe^{2+}, which indicates pseudocapacitive behavior. With the increase of scan rate, the CV curves maintain the overall shape, the anodic peaks shift toward larger potential values, and the cathodic peaks shift toward lower potential values. The shift can be explained by the Randles–Sevcik equation[59] and the increased ionic diffusion resistance at a high scan rate.[60–64]

Galvanostatic charge–discharge (GCD) measurements of the 2D Fe_2O_3/rGO (10/1) nanocomposite at different current densities were also conducted (Fig. 4b). Charging to 0.35 V is completed in a few seconds, followed by a slower charging to 0.47 V. In the discharge curves, there is a plateau at around 0.25 V in low current density measurements, which is characteristic of pseudocapacitive behavior and matches with the reduction peak in CV measurements. The most pronounced plateaus for both 2D MOs were observed in the low current density curves, this is due to the sufficient time that ensure the electrolyte ions to interact with the electrode at a low charging/discharging rate. When the current density increased, the plateaus were obviously shortened since the insufficient time for the ions to reach the entire electrode surface area and the redox reaction become more restricted to the more easy accessible area, which limits the charge storage capability.[65,66]

Moreover, we also studied the electrochemical performance of pristine 2D Fe_2O_3 (without incorporation of graphene oxide during the synthesis) and 2D Fe_2O_3/rGO nanocomposites with different ratios between the two components. The CV scans of 2D Fe_2O_3 and 2D Fe_2O_3/rGO (20/1) are shown in Fig. S4.† Both

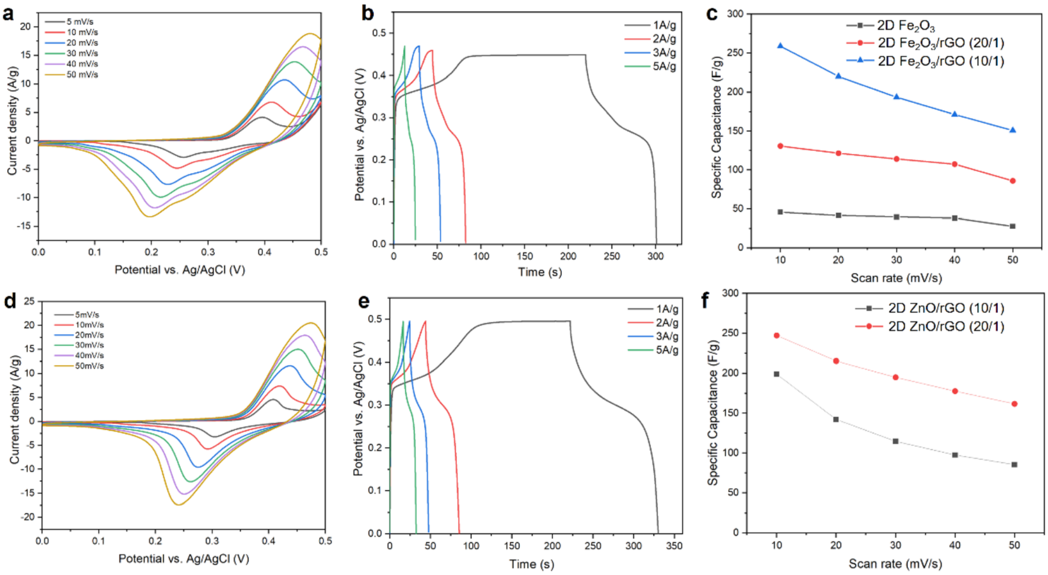

Fig. 4 Electrochemical characterization of 2D MOs and the 2D MO/rGO hybrid materials in a 3-electrode configuration. (a) CV scans of 2D Fe_2O_3/rGO (10/1) in the scan rate range of 5–50 mV s^{-1}. (b) GCD curves at different current densities of 2D Fe_2O_3/rGO (10/1). (c) Comparison of the specific capacitances of 2D Fe_2O_3, 2D Fe_2O_3/rGO (20/1), and 2D Fe_2O_3/rGO (10/1). (d) CV scans of 2D ZnO/rGO (20/1) in the scan rate range of 5–50 mV s^{-1}. (e) GCD curves at different current densities of 2D ZnO/rGO (20/1). (f) Comparison of specific capacitances of 2D ZnO, 2D ZnO/rGO (10/1), and 2D ZnO/rGO (20/1).

samples show similar shapes and peak positions in the CV curves compared with 2D Fe_2O_3/G (10/1), but the current density and area within the CV curves are smaller. The calculated specific capacitance values for the three samples were compared and are presented in Fig. 4c. It can be seen that pristine 2D Fe_2O_3 has the lowest capacitance of 45.7 F g^{-1} (at a scan rate of 10 mV s^{-1}), primarily due to the low electrical conductivity. The two 2D Fe_2O_3/rGO composites have substantially improved capacitance, especially for 2D Fe_2O_3/rGO (10/1), with a capacitance of 258.9 F g^{-1} at 10 mV s^{-1} and 331.4 F g^{-1} at 1 mV s^{-1}, respectively.

The electrochemical capacitance of pristine 2D Fe_2O_3 is limited by its intrinsic low conductivity that limits charge transfer.[13] After the incorporation of rGO, there are three factors that can contribute to the electrochemical performance of the 2D Fe_2O_3/rGO nanocomposites. First, the intercalated hybrid structures with smaller 2D Fe_2O_3 nanosheets on the surface or between rGO flakes increase the electrochemically active sites. The enhanced intercalation and surface accumulation of ions increase the electrochemical kinetics.[14,67] Second, the high conductivity of rGO promotes charge transfer during the reversible charge storage–release process.[65,66] Third, rGO also exhibits a certain extent of pseudocapacitive behavior due to the oxygen-containing groups that can contribute to the overall pseudocapacitive capacitance.[57,68,69]

Our solid-state synthesis approach is versatile and can be used to synthesize other types of 2D MO/rGO composites including 2D ZnO/rGO. The electrochemical properties of the 2D ZnO/rGO nanocomposites were also investigated. The CV curves of 2D ZnO/rGO (20 : 1) at different scan rates are shown in Fig. 4d. A pair of redox peaks located at around 0.25 V and 0.42 V can be observed, which primarily correspond to the intercalation and deintercalation of K^+ from the electrolyte into ZnO ($ZnO + K^+ + e^- \leftrightarrow ZnOK$).[70] GCD tests for 2D ZnO/rGO (20 : 1) at different current densities were also conducted (Fig. 4e). In the discharge curves, there is a plateau at around 0.30 V, which is characteristic of pseudocapacitive behavior and matches with the reduction peak in CV measurements.

We also varied the ratio of ZnO to rGO in the 2D ZnO/rGO nanocomposites. The specific capacitance values for two samples, 2D ZnO/rGO (20 : 1) and 2D ZnO/rGO (10 : 1), are summarized in Fig. 4f (see also Fig. S5†), which shows that the two samples have a capacitance of 247.3 F g^{-1} and 199.0 F g^{-1}, respectively, at a scan rate of 10 mV s^{-1}. Such performance is comparable to the 2D Fe_2O_3/rGO nanocomposite. Due to the higher yield of 2D the Fe_2O_3/rGO nanocomposites in the solid-state synthesis, we will focus the following discussion of supercapacitor devices to those with the 2D Fe_2O_3/rGO electrodes.

We compared the electrochemical performance of our 2D Fe_2O_3/rGO nanocomposites with literature reports on similar material systems composed of iron oxide and carbon nanostructures, including Fe_2O_3@N-doped porous carbon,[71] Fe_3O_4 nanoparticles on rGO,[72] α-Fe_2O_3 nanotube arrays,[73] RGO-Fe_3O_4,[69] Fe_3O_4/MWCNTs,[74] hydrothermal Fe_3O_4 nanoparticles,[75] and Fe_2O_3/3D graphene aerogels.[76] The results are summarized in Fig. S6 and Table S1.† Our 2D Fe_2O_3/rGO nanocomposite has superior specific capacitance (230.1 F g^{-1} capacitance at 1 A g^{-1} from GCD data) compared with others. The excellent electrochemical performance in combination with scalable solid-state synthesis makes the 2D Fe_2O_3/rGO nanocomposites promising candidates as electrode materials for energy storage devices.

3.4 Fabrication and characterization of MSCs based on 2D Fe_2O_3/rGO nanocomposites

Two approaches were used for the fabrication of microsupercapacitors (MSCs) based on the 2D Fe_2O_3/rGO nanocomposites, the first approach is based on photolithography and vacuum filtration and the second approach is based on laser cutting and spray coating. In the first approach, 2D Fe_2O_3/rGO was deposited on filter paper through a photolithography-patterned mask as an interdigitated electrode. PVA/KOH gel electrolyte was then deposited on top of the electrodes. Controlled amount of electrochemically exfoliated graphene (EG) was also mixed with the 2D Fe_2O_3/rGO nanocomposites in the electrodes, because the as-prepared 2D Fe_2O_3/rGO nanocomposite has limited conductivity, which results in a relatively low capacitance of the MSC device (Fig. S7†).

The fabricated MSC device is shown in Fig. 5a, the length of each interdigitated electrode is 4 mm, the width is 0.4 mm, and the gap between neighboring fingers is 0.2 mm. The overall device size is 5.4 × 7.7 mm. The optical microscope image shows the lithography-patterned electrode with a well-defined size and shape. The SEM image of the electrode surface shows a high density of 2D Fe_2O_3/rGO nanoflakes.

CV measurements of the MSC device with an electrode composed of a 2D Fe_2O_3/G and EG mixture (1 : 1 weight ratio) at different scan rates are shown in Fig. 5b. The data show characteristics of both pseudocapacitive and EDLC features originated from the 2D Fe_2O_3/rGO nanocomposites. The redox peaks become less pronounced at scan rates of 50 mV s^{-1} and above. This could be attributed to the limitation of the ion transport rate to the electroactive surface and the more pronounced double-layer charging at high scan rates. The GCD curves of the MSC device are shown in Fig. 5c. At a low current density (such as 0.6 mA cm^{-2}), there is a plateau in the discharge process (potential range of 0.2–0.4 V), which can be attributed to redox process at this range and the rate of which is slower than double-layer discharging. At high current densities, the GCD curves have a symmetric triangle shape without any plateau.

We also studied the effect of incorporating EG into the 2D Fe_2O_3/rGO nanocomposites on the MSC device performance. The electrochemical performance of two types of devices, one using only 2D Fe_2O_3/rGO as the electrodes and the other using 2D Fe_2O_3/rGO mixed with EG (weight ratio 1 : 1) as the electrodes, was compared by plotting their specific capacitance at different scan rates (Fig. 5d). It can be seen that the incorporation of EG effectively increased the capacitance. For instance, the device with the mixture in the electrodes has a capacitance of 35.5 mF cm^{-2} at 5 mV s^{-1}, while the MSC with only 2D Fe_2O_3/rGO in electrodes shows a capacitance of 10.9 mF cm^{-2}

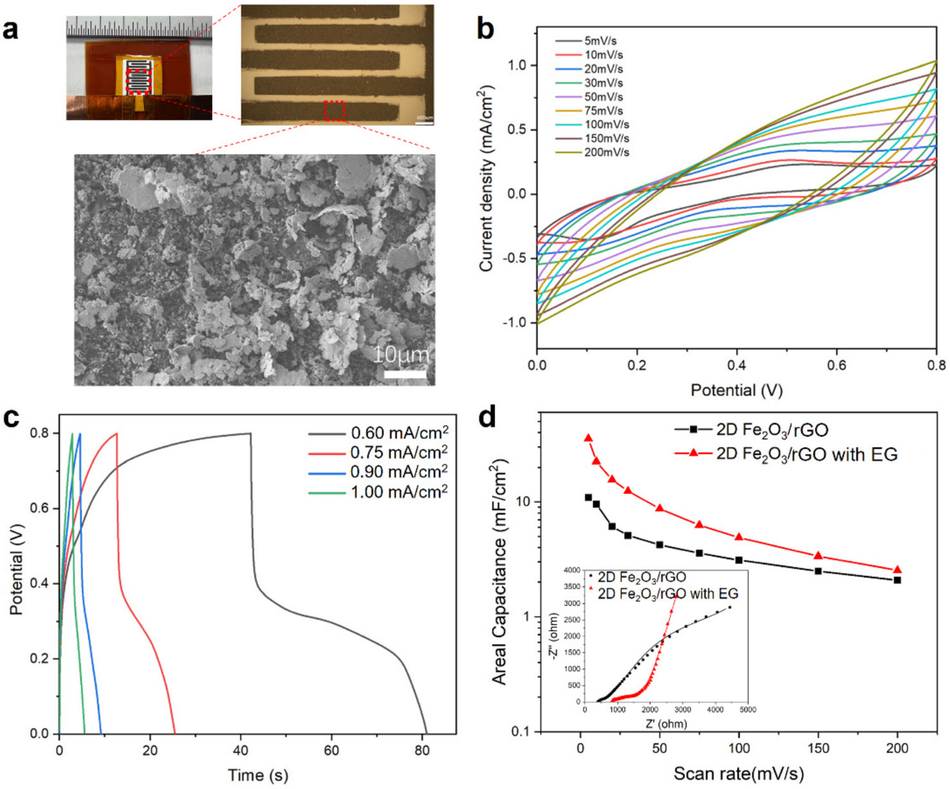

Fig. 5 Electrochemical performance of MSCs with the 2D Fe_2O_3/rGO (10/1) electrode. (a) Photo and optical microscopy image of the MSC device; the SEM image shows that the electrode surface has a high density of 2D nanoflakes. (b) CV scans at different scan rates from 5 mV s^{-1} to 200 mV s^{-1}. (c) GCD curves from 0.6 mA cm^{-2} to 1.0 mA cm^{-2}. (d) Specific capacitance comparison of MSCs with their electrodes compared of either 2D Fe_2O_3/rGO (10/1) or its mixture with EG. The inset shows the Nyquist plots and fitting from EIS measurements.

at the same scan rate. The Nyquist plots of the two devices from EIS measurements and their fitting are shown in the inset (more details are given in Fig. S8 and Table S2†). The MSC with mixture electrodes shows a larger intercept on the real axis and a substantially higher slope in the low-frequency region.[57,77] This result indicates that the enhanced performance of MSC with mixture electrodes is primarily due to the enhanced ion adsorption and diffusion rate, and the increased contribution from the electric double-layer capacitance.

For the symmetric MSC devices discussed above, despite their high resolution fabrication and small form factor, the main limitation is the relatively narrow operation window (0.8 V) due to the symmetric electrodes. In order to expand the operation window, we used another approach, which is based on laser cutting and spray coating, to fabricate asymmetric MSCs. Two different suspensions can be used to spray-coat and fabricate the two different electrodes on each side.

For the asymmetric MSC device shown in Fig. 6a, the interdigital electrodes on the two sides are 2D Fe_2O_3/rGO (10/1) and EG, respectively. The SEM image shows the surface of the electrodes has a high density of loosely connected 2D nanosheets. The CV scans of the two individual electrodes in the half-cell configuration are shown in Fig. 6b, from which the specific capacitances (at a scan rate of 50 mV s^{-1}) of 2D Fe_2O_3/rGO (10/1) and EG were calculated to be 150.8 F g^{-1} and 22.1 F g^{-1}, respectively. The mass of each electrode to be deposited was calculated based on their capacitance to reach charge balance during operation.

CV scans of the asymmetric MSC at different scan rates are shown in Fig. 6c. The operation voltage window substantially increased to 1.5 V. The CV curves show both pseudocapacitive and EDLC features. The GCD data (Fig. 6d) show relatively fast charging and discharge. At a low discharge rate (0.02 mA cm^{-2}), there is a plateau at around 0.25 V in the curve, which corresponds to the redox peak in the CV scan. The area-specific capacitance of the asymmetric MSC is lower than that of the symmetric MSC (for instance, 2.5 mF cm^{-2} *vs.* 35.4 mF cm^{-2} at 10 mV s^{-1} scan rate). The main reason is the loose structure and smaller thickness of the electrodes from the spray coating method, as shown by the SEM image in Fig. 6a, which can lead to less continuity and lower conductivity compared with electrodes prepared by the vacuum filtration method.

To further confirm that such differences in the MSC performance is mainly due to the fabrication method, we fabricated symmetric MSC devices also by the spray coating method using the 2D Fe_2O_3/rGO (10/1) nanocomposites. The

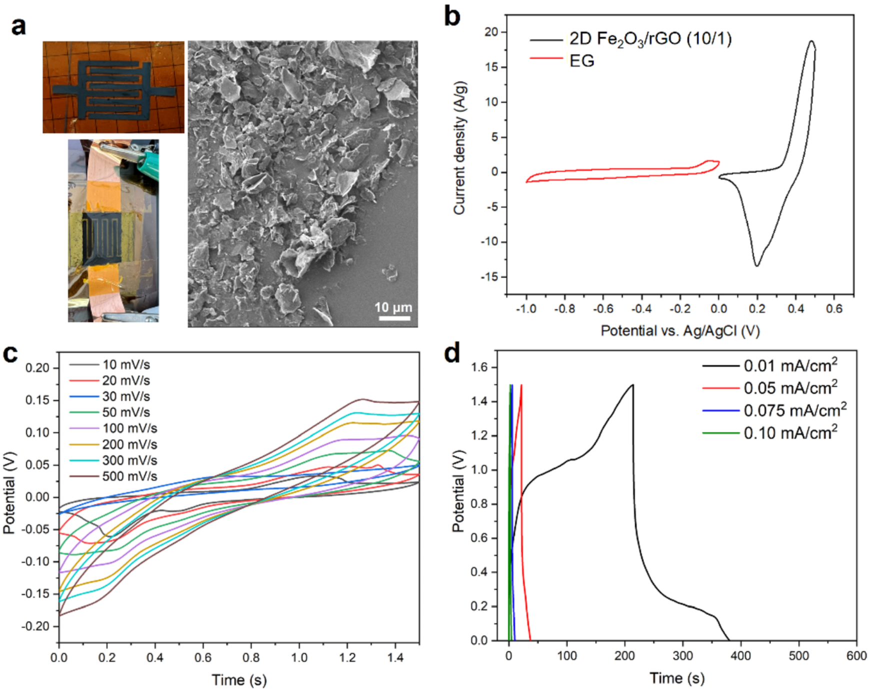

Fig. 6 Electrochemical performance of the asymmetric MSC fabricated with 2D Fe_2O_3/rGO (10/1) as one electrode and EG as the other electrode. (a) Photos of the MSC devices before and during testing. The SEM image on the right shows the surface of the 2D Fe_2O_3/rGO electrode. (b) CV curves of two electrodes tested separately in a half-cell configuration at 50 mV s^{-1}. (c) CV scans of the asymmetric MSC at different scan rates from 10 mV s^{-1} to 500 mV s^{-1}. (d) Charge–discharge curves of the asymmetric MSC at different current densities from 0.01 mA cm^{-2} to 0.1 mA cm^{-2}.

CV scan curves and GCD curves of the MSC are shown in Fig. S9.† Such a device has a much lower capacitance (0.59 mF cm^{-2} at 10 mV s^{-1}) compared with the symmetric MSC fabricated by vacuum filtration (Fig. 5b and c), but close to that of the asymmetric MSC (2.50 mF cm^{-2}) also fabricated by the spray coating method. Such a comparative study also confirms that the asymmetric MSC has higher capacitance due to the enlarged electrochemical operation window.

4. Conclusions

In summary, we have developed a simple, efficient, and scalable method for the synthesis of 2D MO/rGO nanocomposites. Our method is microwave-assisted and conducted in the solid-state without the need for solvents or direct heating. Two-dimensional Fe_2O_3 and ZnO as well as their rGO nanocomposites were successfully obtained. The ratio of 2D MO and rGO components in such 2D nanocomposites can be easily tuned during the solid-state synthesis.

Systematic characterization of these 2D MOs and 2D MO/rGO nanocomposites was conducted using spectroscopies, electron microscopies and diffraction methods. The electrochemical properties of the 2D Fe_2O_3/rGO nanocomposites were investigated, which show an excellent specific capacitance of 331.4 F g^{-1} at a 1 mV s^{-1} scan rate. Such 2D Fe_2O_3/rGO nanocomposites were further used as the main electrode materials to fabricate MSCs. Both symmetric and asymmetric MSCs were fabricated and tested, and their energy storage capability was demonstrated. This work is of high importance to the fields of solid-state chemistry, electrochemistry, and energy storage and has the potential to be used in next-generation supercapacitors and batteries as high-performance electrodes. Our approach is also highly flexible and can be used for the synthesis of mixed MO nanostructures and their graphene nanocomposites. Such multifunctional nanocomposites with multiple types of MOs can have highly tunable band gaps and electrochemical activities for broad applications.

Author contributions

W. X. conceived and supervised the study. M. Y. performed the materials synthesis, device fabrication, and characterization. P. K. and J. B. contributed to materials characterization. All authors contributed to the writing and revision of the manuscript.

Conflicts of interest

There are no conflicts of interest to declare.

Acknowledgements

W. X. gratefully acknowledges the startup support from the University of Akron. This work was also supported by the Firestone Research Initiative Fellowship in the College of Engineering and Polymer Science at the University of Akron.

References

1 M. Winter and R. J. Brodd, *Chem. Rev.*, 2004, **104**, 4245–4270.
2 D. Larcher and J.-M. Tarascon, *Nat. Chem.*, 2015, **7**, 19–29.
3 L. Li Zhang and X. S. Zhao, *Chem. Soc. Rev.*, 2009, **38**, 2520–2531.
4 M. R. Lukatskaya, B. Dunn and Y. Gogotsi, *Nat. Commun.*, 2016, **7**, 12647.
5 J. Jiang, Y. Li, J. Liu, X. Huang, C. Yuan and X. W. (David) Lou, *Adv. Mater.*, 2012, **24**, 5166–5180.
6 C. Guan, X. Li, Z. Wang, X. Cao, C. Soci, H. Zhang and H. J. Fan, *Adv. Mater.*, 2012, **24**, 4186–4190.
7 P. Simon and Y. Gogotsi, *Nat. Mater.*, 2008, **7**, 845–854.
8 W. Zuo, R. Li, C. Zhou, Y. Li, J. Xia and J. Liu, *Adv. Sci.*, 2017, **4**, 1600539.
9 W. Raza, F. Ali, N. Raza, Y. Luo, K.-H. Kim, J. Yang, S. Kumar, A. Mehmood and E. E. Kwon, *Nano Energy*, 2018, **52**, 441–473.
10 A. González, E. Goikolea, J. A. Barrena and R. Mysyk, *Renewable Sustainable Energy Rev.*, 2016, **58**, 1189–1206.
11 M. Cui and X. Meng, *Nanoscale Adv.*, 2020, **2**, 5516–5528.
12 G. Maduraiveeran, M. Sasidharan and W. Jin, *Prog. Mater. Sci.*, 2019, **106**, 100574.
13 C. An, Y. Zhang, H. Guo and Y. Wang, *Nanoscale Adv.*, 2019, **1**, 4644–4658.
14 I. Melkiyur, Y. Rathinam, P. S. Kumar, A. Sankaiya, S. Pitchaiya, R. Ganesan and D. Velauthapillai, *Renewable Sustainable Energy Rev.*, 2023, **173**, 113106.
15 T. Nguyen and M. de F. Montemor, *Adv. Sci.*, 2019, **6**, 1801797.
16 M. Kandasamy, S. Sahoo, S. K. Nayak, B. Chakraborty and C. S. Rout, *J. Mater. Chem. A*, 2021, **9**, 17643–17700.
17 D. Nandi, V. B. Mohan, A. K. Bhowmick and D. Bhattacharyya, *J. Mater. Sci.*, 2020, **55**, 6375–6400.
18 S. Yadav and A. Sharma, *J. Energy Storage*, 2021, **44**, 103295.
19 W. Ma, S. Chen, S. Yang, W. Chen, W. Weng, Y. Cheng and M. Zhu, *Carbon*, 2017, **113**, 151–158.
20 J. Park, K. An, Y. Hwang, J.-G. Park, H.-J. Noh, J.-Y. Kim, J.-H. Park, N.-M. Hwang and T. Hyeon, *Nat. Mater.*, 2004, **3**, 891–895.
21 B. H. Kim, N. Lee, H. Kim, K. An, Y. I. Park, Y. Choi, K. Shin, Y. Lee, S. G. Kwon, H. B. Na, J.-G. Park, T.-Y. Ahn, Y.-W. Kim, W. K. Moon, S. H. Choi and T. Hyeon, *J. Am. Chem. Soc.*, 2011, **133**, 12624–12631.
22 T. Guo, M.-S. Yao, Y.-H. Lin and C.-W. Nan, *CrystEngComm*, 2015, **17**, 3551–3585.
23 R. S. Kate, H. M. Pathan, R. Kalubarme, B. B. Kale and R. J. Deokate, *J. Energy Storage*, 2022, **54**, 105387.
24 U. Cvelbar, Z. Chen, M. K. Sunkara and M. Mozetič, *Small*, 2008, **4**, 1610–1614.
25 S. Vangelista, R. Mantovan, S. Cocco, A. Lamperti, O. Salicio and M. Fanciulli, *Thin Solid Films*, 2012, **520**, 4617–4621.
26 K. Chen, Y.-H. Cao, S. Yadav, G.-C. Kim, Z. Han, W. Wang, W.-J. Zhang, V. Dao and I.-H. Lee, *Chem. Eng. J.*, 2023, **463**, 142396.
27 L. Shi, C. Wu, Y. Wang, Y. Dou, D. Yuan, H. Li, H. Huang, Y. Zhang, I. D. Gates, X. Sun and T. Ma, *Adv. Funct. Mater.*, 2022, **32**, 2202571.
28 D. Yuan, Y. Dou, Y. Tian, D. Adekoya, L. Xu and S. Zhang, *Angew. Chem., Int. Ed.*, 2021, **60**, 18830–18837.
29 Y. Dou, D. Yuan, L. Yu, W. Zhang, L. Zhang, K. Fan, M. Al-Mamun, P. Liu, C.-T. He and H. Zhao, *Adv. Mater.*, 2022, **34**, 2104667.
30 A. Puthirath Balan, S. Radhakrishnan, C. F. Woellner, S. K. Sinha, L. Deng, C. de los Reyes, B. M. Rao, M. Paulose, R. Neupane, A. Apte, V. Kochat, R. Vajtai, A. R. Harutyunyan, C.-W. Chu, G. Costin, D. S. Galvao, A. A. Martí, P. A. van Aken, O. K. Varghese, C. S. Tiwary, A. Malie Madom Ramaswamy Iyer and P. M. Ajayan, *Nat. Nanotechnol.*, 2018, **13**, 602–609.
31 A. Koutsioukis, G. Florakis, N. Samartzis, S. N. Yannopoulos, M. Stavrou, D. Theodoropoulou, N. Chazapis, S. Couris, A. Kolokithas-Ntoukas, G. Asimakopoulos, D. P. Gournis, V. Tzitzios, E. Sakellis, S. F. Tombros, S. Kokkalas and V. Georgakilas, *J. Mater. Chem. C*, 2023, **11**, 3244–3251.
32 S. Chahal, S. M. Kauzlarich and P. Kumar, *ACS Mater. Lett.*, 2021, **3**, 631–640.
33 J. Dzíbelová, S. M. H. Hejazi, V. Šedajová, D. Panáček, P. Jakubec, Z. Baďura, O. Malina, J. Kašlík, J. Filip, Š. Kment, M. Otyepka and R. Zbořil, *Appl. Mater. Today*, 2023, **34**, 101881.
34 M. Stavrou, N. Chazapis, V. Arapakis, V. Georgakilas and S. Couris, *ACS Appl. Mater. Interfaces*, 2023, **15**, 35391–35399.
35 R. Singla, T. A. Hackett, S. Kumar, J. Sharma and M. K. Kashyap, *Nanoscale Adv.*, 2020, **2**, 5890–5896.
36 Y. Wei, M. Ghorbani-Asl and A. V. Krasheninnikov, *J. Phys. Chem. C*, 2020, **124**, 22784–22792.
37 D. Chen, G. Zhang, W. Sun, J. Li, Z. Cheng and Y. Wang, *Phys. Chem. Chem. Phys.*, 2019, **21**, 12301–12309.
38 B. Y. Zhang, K. Xu, Q. Yao, A. Jannat, G. Ren, M. R. Field, X. Wen, C. Zhou, A. Zavabeti and J. Z. Ou, *Nat. Mater.*, 2021, **20**, 1073–1078.
39 Z. Zhang, D. Vieira, J. E. Barralet and G. Merle, *2D Mater.*, 2020, **7**, 025044.
40 J. Chen, B. Yao, C. Li and G. Shi, *Carbon*, 2013, **64**, 225–229.
41 Y. Chen, S. Zhang, Y. Feng, G. Yang, H. Ji and X. Miao, *ChemElectroChem*, 2020, **7**, 5013–5020.

42 H. Quan, B. Cheng, Y. Xiao and S. Lei, *Chem. Eng. J.*, 2016, **286**, 165–173.

43 D. L. A. de Faria, S. Venâncio Silva and M. T. de Oliveira, *J. Raman Spectrosc.*, 1997, **28**, 873–878.

44 K. F. McCarty, *Solid State Commun.*, 1988, **68**, 799–802.

45 J.-W. Jang, C. Du, Y. Ye, Y. Lin, X. Yao, J. Thorne, E. Liu, G. McMahon, J. Zhu, A. Javey, J. Guo and D. Wang, *Nat. Commun.*, 2015, **6**, 7447.

46 A. Momot, M. N. Amini, G. Reekmans, D. Lamoen, B. Partoens, D. R. Slocombe, K. Elen, P. Adriaensens, A. Hardy and M. K. Van Bael, *Phys. Chem. Chem. Phys.*, 2017, **19**, 27866–27877.

47 C. J. Raj, R. K. Joshi and K. B. R. Varma, *Cryst. Res. Technol.*, 2011, **46**, 1181–1188.

48 X. Dong, Y. Cao, J. Wang, M. B. Chan-Park, L. Wang, W. Huang and P. Chen, *RSC Adv.*, 2012, **2**, 4364.

49 N. M. S. Hidayah, W.-W. Liu, C.-W. Lai, N. Z. Noriman, C.-S. Khe, U. Hashim and H. C. Lee, *AIP Conf. Proc.*, 2017, **1892**, 150002.

50 C. Sun, S. Liu, X. Shi, C. Lai, J. Liang and Y. Chen, *Chem. Eng. J.*, 2020, **381**, 122641.

51 A. Thejas Prasannakumar, C. Beryl, R. Rohith, U. R. Felscia, R. Philip and S. J. Varma, *ACS Appl. Opt. Mater.*, 2023, **1**, 660–668.

52 H. Quan, B. Cheng, Y. Xiao and S. Lei, *Chem. Eng. J.*, 2016, **286**, 165–173.

53 D. Flak, Q. Chen, B. S. Mun, Z. Liu, M. Rękas and A. Braun, *Appl. Surf. Sci.*, 2018, **455**, 1019–1028.

54 P. Zhao, W. Li, G. Wang, B. Yu, X. Li, J. Bai and Z. Ren, *J. Alloys Compd.*, 2014, **604**, 87–93.

55 M. Sathyan, P. J. Jandas and H. John, *Electrochim. Acta*, 2024, **474**, 143576.

56 M. Sathyan, P. J. Jandas, M. Venkatesan, S. C. Pillai and H. John, *Synth. Met.*, 2022, **287**, 117080.

57 R. Kumar, S. M. Youssry, E. Joanni, S. Sahoo, G. Kawamura and A. Matsuda, *J. Energy Storage*, 2022, **56**, 105896.

58 X. Lu, Y. Zeng, M. Yu, T. Zhai, C. Liang, S. Xie, M.-S. Balogun and Y. Tong, *Adv. Mater.*, 2014, **26**, 3148–3155.

59 N. Elgrishi, K. J. Rountree, B. D. McCarthy, E. S. Rountree, T. T. Eisenhart and J. L. Dempsey, *J. Chem. Educ.*, 2018, **95**, 197–206.

60 K. J. Aoki, J. Chen, Y. Liu and B. Jia, *J. Electroanal. Chem.*, 2020, **856**, 113609.

61 E. M. Espinoza, J. A. Clark, J. Soliman, J. B. Derr, M. Morales and V. I. Vullev, *J. Electrochem. Soc.*, 2019, **166**, H3175.

62 M. Aadil, S. Zulfiqar, M. Shahid, P. O. Agboola, N. F. Al-Khalli, M. F. Warsi and I. Shakir, *Electrochim. Acta*, 2021, **383**, 138332.

63 V. Vedharathinam and G. G. Botte, *Electrochim. Acta*, 2012, **81**, 292–300.

64 A. Phakkhawan, P. Suksangrat, P. Srepusharawoot, S. Ruangchai, P. Klangtakai, S. Pimanpang and V. Amornkitbamrung, *J. Alloys Compd.*, 2022, **919**, 165702.

65 J. Lee, T. S. Lim, S. G. Jo, S. Jeong, H. Paik, I. W. Ock, S. Lee, K. J. Yu and J. W. Lee, *Chem. Eng. J.*, 2023, **476**, 146515.

66 A. Mumtaz, J. Iqbal and M. Oneeb, *J. Energy Storage*, 2023, **74**, 109320.

67 M. Geerthana, S. Prabhu, S. Harish, M. Navaneethan, R. Ramesh and M. Selvaraj, *J. Mater. Sci.: Mater. Electron.*, 2022, **33**, 8327–8343.

68 Z.-D. Huang, B. Zhang, R. Liang, Q.-B. Zheng, S. W. Oh, X.-Y. Lin, N. Yousefi and J.-K. Kim, *Carbon*, 2012, **50**, 4239–4251.

69 S. Ghasemi and F. Ahmadi, *J. Power Sources*, 2015, **289**, 129–137.

70 K. Hassan, R. Farzana and V. Sahajwalla, *SN Appl. Sci.*, 2019, **1**, 302.

71 D. Cai, J. Du, C. Zhu, Q. Cao, L. Huang, J. Wu, D. Zhou, Q. Xia, T. Chen, C. Guan and Y. Xia, *ACS Appl. Energy Mater.*, 2020, **3**, 12162–12171.

72 Q. Wang, L. Jiao, H. Du, Y. Wang and H. Yuan, *J. Power Sources*, 2014, **245**, 101–106.

73 K. Xie, J. Li, Y. Lai, W. Lu, Z. Zhang, Y. Liu, L. Zhou and H. Huang, *Electrochem. Commun.*, 2011, **13**, 657–660.

74 M. Krajewski, P.-Y. Liao, M. Michalska, M. Tokarczyk and J.-Y. Lin, *J. Energy Storage*, 2019, **26**, 101020.

75 L. Wang, H. Ji, S. Wang, L. Kong, X. Jiang and G. Yang, *Nanoscale*, 2013, **5**, 3793–3799.

76 Z. Song, W. Liu, P. Xiao, Z. Zhao, G. Liu and J. Qiu, *Mater. Lett.*, 2015, **145**, 44–47.

77 A. Ray, J. Roth and B. Saruhan, *Molecules*, 2022, **27**, 329.